Journal of the Physical Society of Japan **94**, 101004 (2025)
https://doi.org/10.7566/JPSJ.94.101004

Special Topics
Recent Progress in Topological Photonics and Related Fields

Mid-IR Electromagnetic Topological Edge Modes: Design, Fabrication, and Polarization States Confirmed by High-Angle-Resolution Reflection Spectroscopy

Yuanzhao Yao[1], Afshan Begum[2], Naoki Ikeda[3], Yoshihiko Takeda[4],
Takashi Kuroda[2], and Kazuaki Sakoda[2]*

[1]*Department of Applied Physics, University of Tsukuba, Tsukuba, Ibaraki 305-8573, Japan*
[2]*Research Center for Functional Materials, National Institute for Materials Science, Tsukuba, Ibaraki 305-0044, Japan*
[3]*Research Network and Facility Service Division, National Institute for Materials Science, Tsukuba, Ibaraki 305-0047, Japan*
[4]*Center for Green Research on Energy and Environmental Materials, National Institute for Materials Science,*
Tsukuba, Ibaraki 305-0003, Japan

(Received November 19, 2024; accepted March 17, 2025; published online July 24, 2025)

We review our recent studies on the design, fabrication, and experimental verification by angle-resolved reflection spectroscopy of topological photonic crystals (PhCs) and topologically protected edge modes in the mid-infrared frequency range. We adopted a sample design based on the symmetry reduction from the honeycomb lattice to the C_{6v}-symmetric lattice to tune the frequencies of E_1- and E_2-symmetric eigenmodes on the Γ point of the Brillouin zone. In addition to topologically trivial and non-trivial band gaps, we also succeeded in observing double Dirac cones with an isotropic linear dispersion relation by accidental degeneracy of the E_1- and E_2-symmetric modes. Our specimens had simple structures of PhC slabs fabricated in SOI (silicon-on-insulator) wafers without under-etching of a sacrificial layer beneath the PhC. Therefore, the photonic band gaps are generally narrow due to the small contrast of refractive indexes. Nevertheless, we achieved a sufficiently wide band gap of 6% relative to the midgap frequency, which facilitated our observation of the edge modes. We also verified experimentally that the edge modes were linearly polarized on the Γ point due to the 1 : 1 mixture of the original left- and right-circular polarizations. All these experimental observations were achieved by using our home-made reflection measurement apparatus with a 0.3° angle resolution.

1. Introduction

The 2016 Nobel Prize in Physics was awarded to David J. Thouless, F. Duncan M. Haldane, and J. Michael Kosterlitz for their theoretical discovery of topological phase transitions and topological phases of matter.1) The topological nature of matter gives rise to a number of interesting physical properties, a prime example of which is the topologically protected edge mode.2,3) They are special electronic states that occur at the boundary between two crystals with different topological properties, where there is a one-to-one correspondence between the spin orientation and the direction of motion, known as spin-momentum locking. Namely, up-spin electrons flow only in one direction along the boundary, whereas down-spin electrons flow only in the reverse direction, creating unprecedented one-way states.

Topological properties are not limited to electrons but are common to all waves in periodic structures. For electromagnetic waves, periodic dielectric structures known as photonic crystals (PhCs)4–9) can imitate topological insulators.10–14) Electromagnetic one-way edge modes can also be materialized on the boundary between topologically trivial and non-trivial PhCs.15–23)

PhCs are often designed to work in visible to infrared frequency ranges where strong interactions between the electromagnetic waves and matter lead to a variety of optical phenomena that result in many important applications such as lasers and sensors. The lattice constant of the PhCs must match the wavelengths of the electromagnetic waves, so it should be of the order of 1 µm.

We need nanofabrication technologies to make PhCs in these frequency ranges, and those PhCs are often fabricated on semiconductor wafers by electron beam (EB) lithography. The semiconductor wafer is basically composed of a substrate and two thin layers on it. The top semiconductor (GaAs, Si, etc.) layer with a large refractive index is the main body of the PhC, in which periodic structures (often air holes) are drawn by EB lithography. The second layer consists of a semiconductor or insulator with a low refractive index. Thus, electromagnetic waves are confined to the top layer, where they are efficiently influenced by periodic modulation of the refractive index. The dispersion relation is therefore strongly modified to materialize band gaps in the electromagnetic spectrum. PhCs of this type are referred to as PhC slabs.

Wu and Hu15) recently reported a design of topological PhCs and edge modes based on symmetry reduction from the honeycomb symmetry to the C_6 symmetry. They introduced a pseudo-time-reversal operator that relies on the C_6 crystal symmetry and showed that they can define pseudo spins consisting of the basis functions of the E' and E'' irreducible representations on the Γ point. The pseudo spin corresponds to the circular polarization of the electromagnetic eigenmode. They further showed by numerical calculation that photonic band gaps can be created by appropriately designing the PhC unit cell. By the $\mathbf{k} \cdot \mathbf{P}$ perturbation around the Γ point, they showed that the Chern number is non-zero, and so the band gap is topologically non-trivial when the E'-mode frequency is larger than the E''-mode frequency. They also confirmed the presence of the edge modes on the boundary between two PhCs with trivial and non-trivial band gaps by numerical calculations. Topological PhC slabs were studied both theoretically and experimentally according to their idea.16–23)

In this review, we report our recent studies on topological PhCs fabricated in silicon-on-insulator (SOI) wafers, which is a platform for highly developed silicon photonics. We followed the sample design by Wu and Hu.15) Based on the numerical design by finite element method (FEM) calculations, we fabricated SOI PhC slabs by EB lithography that materialized topologically non-trivial band gaps and edge modes. These properties were verified by angle-resolved

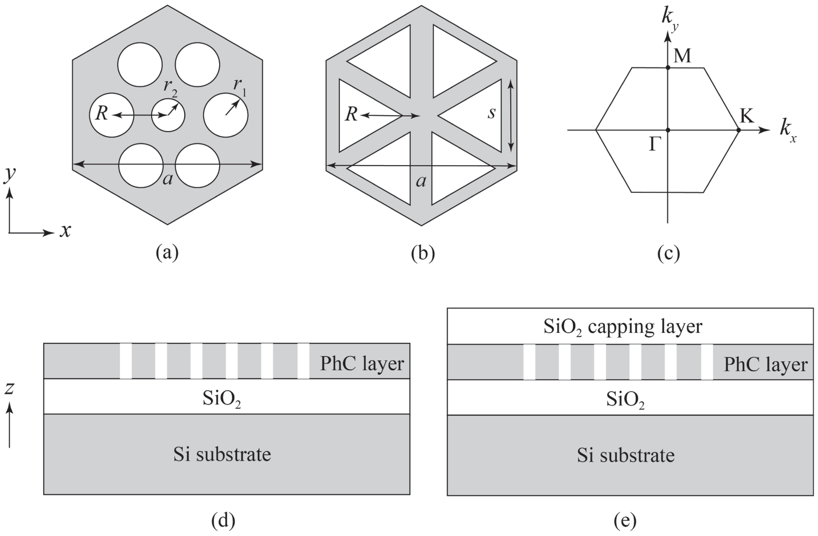

(a) (b) (c)

(d) (e)

Fig. 1. Top views of the unit cell of (a) the seven-hole PhC for observation of the double Dirac cone and (b) the PhC with a topologically trivial or non-trivial band gap, where a is the lattice constant, r_1 and r_2 are the radii of circular air cylinders, R is the distance between the center of the air cylinder and the center of the unit cell, and s is the side length of triangular air cylinders. (c) The first Brillouin zone of the PhC specimens of the C_{6v} symmetry. Side views of (d) asymmetric and (e) symmetric PhCs, where the PhC structure was fabricated in the top silicon layer of SOI wafers. For the symmetric PhCs, the triangular air holes were filled with SiO_2 and a sufficiently thick SiO_2 capping layer was formed.

reflection spectroscopy in the mid-infrared (IR) range by an Fourier-transform infrared (FT-IR) spectrometer for which we newly developed a reflection measurement apparatus with a 0.3° angle resolution. We also examined double Dirac cones materialized by accidental degeneracy of the relevant eigenmodes; the method used was also based on symmetry reduction. We further discuss the incompleteness of the topological band gaps materialized with PhC slabs, and present a method to resolve this problem.

This paper is organized as follows. In Sect. 2, we present the sample design of the seven-hole PhC to observe the double Dirac cone and two topological PhCs to observe the edge modes. Selection rules for the reflection spectroscopy and the polarization of the edge modes are also presented. Sample fabrication is described in Sect. 3. The method used to observe the bulk and edge modes is described in Sect. 4. The results of the measurements are presented in Sect. 5. A brief summary is given in Sect. 6.

2. Sample Design

2.1 *Double Dirac cone*

We previously showed by the $\mathbf{k} \cdot \mathbf{p}$ perturbation theory and a group-theoretical analysis that accidental degeneracy of E_1 and E_2 modes of the C_{6v}-symmetric PhC materializes the double Dirac cone on the Γ point of the Brillouin zone.[24] Although these modes are naturally degenerate by symmetry in the honeycomb lattice, the Dirac cone is located not on the Γ point but on the K point. So, we cannot observe it by reflection spectroscopy because of the mismatch between the lateral component of the wave vector of the incident wave and the PhC eigenmode. To locate the double Dirac cone on the Γ point, we have to reduce the structural symmetry of the PhC from the honeycomb symmetry to the C_{6v} symmetry. Thus, we can make the first Brillouin zone smaller and can fold back the dispersion curves to the zone center.[25]

For this purpose, we start from the honeycomb lattice consisting of circular air cylinders fabricated in the top silicon layer of SOI wafers as shown in Fig. 1(a), where a is the lattice constant and R is the distance between the center of the air cylinder and the center of the unit cell. Here, we also show the unit cell of topological PhCs in Fig. 1(b), which will be described in detail in Sect. 2.2, whereas Fig. 1(c) is the first Brillouin zone of the C_{6v}-symmetric lattice.

When the air cylinder with radius r_2 in the center of the unit cell is absent and $R = a/3$, the six air cylinders with radius r_1 arranged in six-fold rotational symmetry constitute a honeycomb lattice. We reduce the symmetry by shifting the positions of the six air cylinders. Specifically, we set $a = 2.4\,\mu m$, $R = 792\,nm$, and $r_1 = 336\,nm$. We also assume that the top silicon layer, in which the PhC structure is fabricated, is 400 nm thick and is separated by a 3-μm-thick SiO_2 layer from the Si substrate according to the structure of SOI wafers (SOITEC) used in this study [Fig. 1(d)]. At this step, the E_1 and E_2 modes are not degenerate to each other. So, we make them degenerate again by introducing one more air cylinder into the unit-cell center. Because the electric-field distributions of the two modes are sufficiently different from each other, their frequency shifts caused by the seventh air cylinder, which are approximately proportional to the electric-field intensity inside the cylinder, are also different, so we can make their eigen frequencies coincide by adjusting r_2.

We calculated the dispersion relation by FEM software (COMSOL Multiphysics with the Wave Optics Module) and found that the E_1 and E_2 modes were degenerate when $r_2 = 104.4\,nm$.[26] Figure 2 is the dispersion relation around the Γ point, which clearly shows the presence of the double Dirac cone at normalized frequency $\omega a/2\pi c = 0.646$. Note that, in the Γ-to-K direction, two bands are nearly degenerate over the wave vector range of this figure for both upper and lower branches, so they look like single lines. For numerical calculations by FEM, we imposed the perfectly matched layer (PML) absorbing boundary conditions in the vertical (z) direction and the Bloch boundary condition in the lateral (x

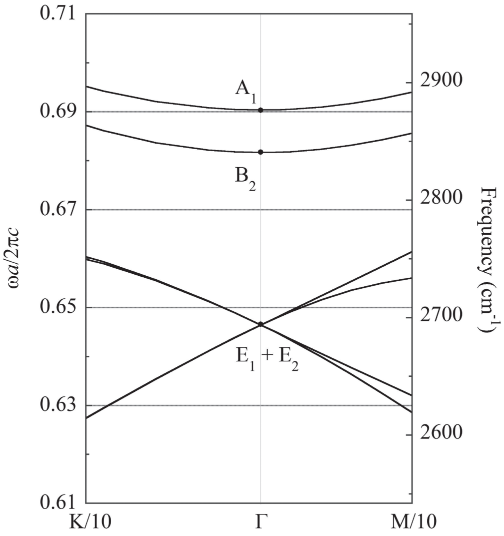

Fig. 2. Dispersion relation of TE-like modes for the seven-hole PhC. The left vertical axis is the normalized frequency, where ω is the angular frequency, a is the lattice constant, and c is the light velocity in free space. The horizontal axis is the wave vector in the Γ-to-K and Γ-to-M directions, where K/10 and M/10 imply that the horizontal axis is magnified 10 times. This figure is taken from Ref. 26. ©2022 The Author(s).

Table I. Selection rules of reflection peaks for the C_{6v}-symmetric PhCs, for which there are six irreducible representations, A_1, A_2, B_1, B_2, E_1, and E_2, on the Γ point. p and s denote that the modes are active to the p and s polarizations, respectively. The E_1 and E_2 modes are doubly degenerate, so there are two branches for each of them in both the Γ-to-K and Γ-to-M directions. One branch is active to the s polarization and the other is active to the p polarization.

Mode on the Γ point	Γ	Γ-to-K	Γ-to-M
A_1	inactive	s	s
A_2	inactive	p	p
B_1	inactive	s	p
B_2	inactive	p	s
E_1	active	s, p	s, p
E_2	inactive	s, p	s, p

and y) directions on the surface of the unit cell to specify the two-dimensional wave vector **k**.

In addition to the double Dirac cone created by the E_1 and E_2 modes, we found an A_1 mode and a B_2 mode in the frequency range of this figure. All of them had TE (transverse electric)-like polarization; that is, their main electric-field components were parallel to the horizontal xy plane. Note that the electric field is a genuine vector, whereas the magnetic field is an axial vector, so their spatial symmetries are generally different from each other.[9] In this paper, we denote the symmetry of the magnetic field.

Because the C_{6v}-symmetric lattice is mirror symmetric about both the xz and yz planes, the electromagnetic eigenmodes on the Γ-to-K and Γ-to-M directions, respectively, have parity for these mirror planes. This parity leads to polarization selection rules for reflection spectroscopy as listed in Table I, where s and p imply that the eigenmode is active to s- and p-polarized incident waves, respectively. The E_1 and E_2 modes are doubly degenerate, so they connect with two dispersion curves in both the Γ-to-K and Γ-to-M directions. One of them is active to the s polarization and the other is active to the p polarization. On the other hand, two plane waves incident from the normal direction ($k_x = k_y = 0$) and polarized in the x and y directions, respectively are basis functions of the E_1 representation.[9] So, they can connect only with the E_1 mode in the PhC. This implies that only the E_1 mode is active to the incident wave on the Γ point. The reflection spectra can be calculated by FEM,[25] and we can confirm these selection rules. They are very powerful for identifying the mode symmetry in angle-resolved reflection spectroscopy, as will be discussed later.

2.2 *Asymmetric topological PhCs*

In the case of topological PhCs for observing edge modes, we need to materialize topologically trivial and non-trivial photonic band gaps over the entire Brillouin zone. In addition, we would like to fabricate them in the top Si layer of the SOI wafers because of the ease of sample fabrication and the affinity for highly developed silicon photonics. Although it is generally believed that air-bridge PhCs, or PhC membranes, are advantageous for materializing large band gaps,[27–29] we looked for non-membrane PhCs, or PhC slabs, to materialize the edge modes.

In early studies of the topological edge modes of PhCs, Barik et al.[16,17] fabricated PhC membranes in thin GaAs layers. They grew AlGaAs (sacrificial layer) and GaAs thin layers on a GaAs wafer and made a periodic array of air cylinders in the top GaAs layer by EB lithography, which is the main body of the PhC. Then, they removed the AlGaAs layer beneath the PhC by selective etching. Thus they obtained the PhC membrane that was suspended in the air. Because the contrast of the refractive index between GaAs and air is large, the electromagnetic eigenmodes of the PhC membrane are efficiently confined to the PhC and its dispersion relation is strongly modified, leading to large band gaps. In fact, Barik et al. materialized a band gap common to topologically trivial and nontrivial PhCs whose frequency width was as large as 4.1% relative to the mid-gap frequency. They further fabricated InAs quantum dots on the PhC and confirmed the one-way propagation of the edge modes by observing the two Zeeman components of the luminescence from the InAs quantum dots under a static magnetic field.[16]

Although the PhC membranes have these excellent properties, they are generally fragile, their fabrication process is rather complicated, and materials applicable to selective etching are limited. For these reasons, researchers have also been trying to materialize and observe the edge modes with PhC slabs without under-etching of the sacrificial layer. For example, Okada et al.[23] fabricated SOI PhC slabs and reported variation of the dispersion curves of topologically trivial and non-trivial PhCs due to the changes in their structural parameters.

The original idea of the topologically non-trivial band gap and edge modes proposed by Wu and Hu[15] was concerned with transverse-magnetic (TM) modes in purely two-dimensional PhCs, which are mathematical model structures consisting of a two-dimensional array of circular dielectric cylinders with an infinite height. This situation can approximately be realized, for example, for PhCs with sufficiently tall Si pillars fabricated on sapphire substrates.[21] On the other hand, air cylinders formed in dielectric slabs were preferred for PhC membranes because the unit cells are

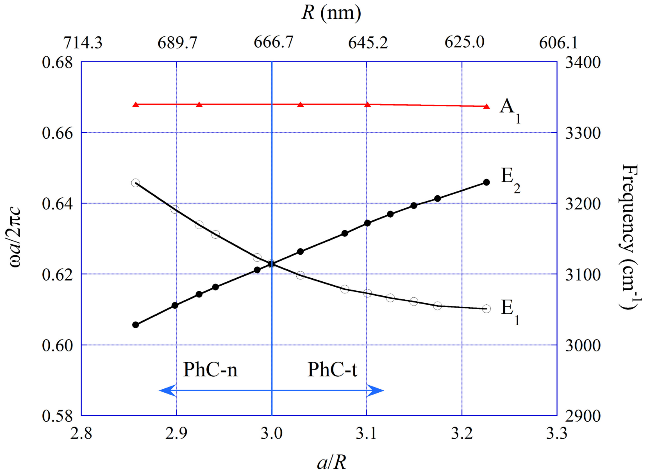

Fig. 3. (Color online) R dependence of the eigen frequencies for asymmetric topological PhCs. a and s were fixed at 2.0 μm and 800 nm, respectively. The E_1 and E_2 modes on the Γ point are plotted with open and solid black circles, respectively. The A_1 mode on the M point is plotted with solid red triangles. For a/R smaller (larger) than three, the gap is non-trivial (trivial). This figure is taken from Ref. 26. ©2022 The Author(s).

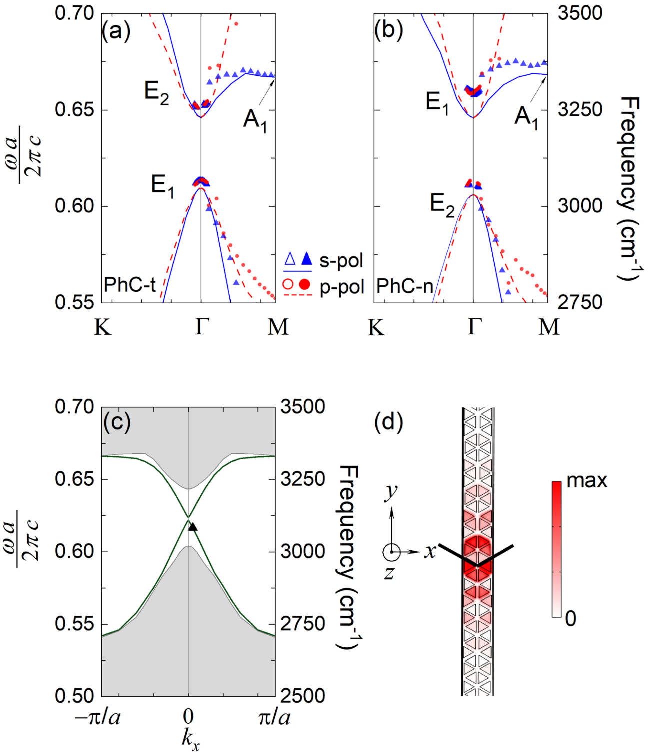

Fig. 4. (Color online) Dispersion relation of the TE-like modes for (a) asymmetric PhC-t and (b) asymmetric PhC-n. Solid and broken lines are dispersion curves for s- and p-active modes, respectively. Open circles and triangles are data points measured by our high angle-resolution reflection apparatus for the s and p polarizations, respectively, whereas solid circles and triangles are those measured by a commercial reflection module (Seagull) for the s and p polarizations, respectively. The following structural parameters were assumed: $a = 2.0\,\mu m$, $s = 800\,nm$, $R = 620\,nm$ for PhC-t and $R = 700$ nm for PhC-n. The refractive indices of Si and SiO_2 were assumed to be 3.427[32] and 1.440,[33] respectively. (c) Dispersion relation of the edge modes (solid lines) and the spectral range of bulk modes (gray regions). The edge-mode dispersion was calculated by assuming 11 unit cells of PhC-t on the upper side ($y > 0$) and of PhC-n on the lower side ($y < 0$) of the boundary along the x axis. We assumed the Bloch boundary condition in the x direction and the PML absorbing boundary conditions in the y and z directions. In each panel, the vertical axes are the genuine (right) and normalized (left) frequencies, whereas the horizontal axis is the wave vector in the first Brillouin zone. k_x denotes the x component of the wave vector. (d) Time-averaged intensity of the z component of the magnetic field plotted for the edge mode denoted by the solid triangle in panel (c). This figure is taken from Ref. 31. ©2023 The Author(s).

naturally connected even in the suspended structure. In this case, photonic band gaps can easily be created in the spectrum of the TE-like modes.

To achieve non-trivial band gaps, Barik et al.[16,17] chose a deformed honeycomb lattice consisting of triangular air cylinders arranged in six-fold rotational symmetry, as shown in Fig. 1(b). In accordance with the idea of Wu and Hu, they confirmed the trivial and non-trivial band gaps in their PhC membranes by decreasing and increasing the distance R, respectively. They adopted the triangular cylinders to prevent the band gap from closing because of the frequency decrease of the A_1 mode on the M point of the Brillouin zone.

Then, we tried to find SOI PhC slab structures that would materialize trivial and non-trivial band gaps by calculating the dispersion relation. We adopted deformed honeycomb-lattice PhCs as in previous studies.[15–23] Figure 3 shows the variation of the eigen frequencies of the E_1 and E_2 modes on the Γ point and the A_1 mode on the M point. As will be described in Sect. 3, we fabricated PhC specimens with $a = 2.0\,\mu m$ and $s = 800\,nm$.[30,31] The dispersion relation was calculated by assuming these values. For $a/R = 3$, the PhC has the honeycomb symmetry and the E_1 and E_2 modes are degenerate. When R is varied, the degeneracy is lifted and a band gap appears. For $a/R > 3$ ($a/R < 3$), the E_2 (E_1) mode frequency is higher, so, according to Wu and Hu,[15] the band gap is topologically trivial (non-trivial). We should note that the eigen frequency of the A_1 mode is higher than the band gap frequency for all a/R assumed in this calculation, which assures that the band gap is open over the entire Brillouin zone.

As we will describe in Sect. 3, we fabricated two topological PhC slabs with $R = 620$ and 700 nm. The former (latter) has a trivial (non-trivial) band gap, so we denote it as PhC-t (PhC-n). They share a common band gap for the TE-like modes whose width is 5.7% relative to the mid-gap frequency. This value is larger than those of the PhC membranes, which are 4.1% in Ref. 17 and 4.7% in Ref. 22, despite the smaller refractive-index contrast of the present specimens. This is because the band gap is governed not only by the refractive-index contrast but also by the amount of the symmetry breaking described by R for the PhCs of the deformed honeycomb structure.

Figures 4(a) and 4(b) show the calculated dispersion relation of PhC-t and PhC-n for the TE-like modes (solid and broken lines) and the experimental observations (circles and triangles), the latter of which will be described later. The eigen frequency of the A_1-symmetric mode on the M point is larger than the E_1 and E_2 mode frequencies on the Γ point, so the band gaps are open over the entire Brillouin zone. Because of the band gap common to the PhC-t and PhC-n, which is a prerequisite for the presence of the edge modes, we can materialize the topologically protected edge modes on the boundary between the two PhCs due to the bulk-edge correspondence.[15] Their dispersion curves are presented by the solid lines in Fig. 4(c), whereas the gray regions denote the frequency ranges of the bulk modes.

We would like to mention three features expected for the edge modes here. First, the edge-mode wave function is localized on the boundary between the two PhCs, as shown in Fig. 4(d). This figure illustrates the top view of one row of the combination specimen, where the upper half is PhC-t and the lower half is PhC-n. The big black wedge denotes their boundary, and this structure is repeated in the x direction. The time-averaged intensity of the z component of the magnetic field is illustrated in red, which is apparently localized on the boundary. Note that because the bulk modes are TE-like polarized, the edge mode has the same polarization, so the z component is the largest component of the magnetic field vector. Also note that we assumed a zigzag boundary between the two PhCs. The localization length of the edge mode was estimated to be 3.6 times the lattice constant.

Secondly, the two dispersion curves of the edge mode have a small gap of $12\,\mathrm{cm}^{-1}$ at $k_x = 0$, which originates from the mode mixing due to the lack of inversion symmetry around the boundary.[15] Each branch is originally characterized by a pseudo spin, which corresponds to the spin angular momentum in the case of electronic systems. In the electromagnetic case, it is related to the circular polarization of the eigenmodes. Then, because of the 1 : 1 mixture of the right and left circular polarizations, it is expected that each branch is characterized by a linear polarization at $k_x = 0$, whereas the polarization returns to the original circular polarization as $|k_x|$ becomes large. Because the electromagnetic field of the edge mode is strongly modulated by the periodic structure of the PhC in the vicinity of the top Si layer, it is rather easy to observe the polarization at positions far away from the top Si layer.

Figure 5 shows the far-field polarization of the edge modes. Each panel shows the endpoint of the electric field vector during one period of the electromagnetic-field oscillation. Because the vicinity of $k_x = 0$ is important, the polarization was examined for $0 \leq k_x \leq 0.008 \times 2\pi/a$. As Figs. 5(a) and 5(b) show, the far field is linearly polarized at $k_x = 0$ for both the lower and upper branches. We can confirm these linear polarizations by reflection spectroscopy, as will be discussed in Sect. 5.

Thirdly, the topological band gaps described in this section are related to bulk modes with the TE-like polarization. On the other hand, there are TM-like bulk modes in the frequency range of the topological band gaps. This means that the band gaps are incomplete. Nonetheless, we found the edge modes by numerical calculations and by reflection measurements, as will be described in Sect. 5. This finding is most probably brought about by the small mixing between the TE- and TM-like modes even in the presence of the imperfections destroying the structural periodicity associated with the boundary between the two PhCs. We think that this issue needs further investigation, since the incompleteness of the band gap is a new feature unique to topological photonics.

Regarding this issue, we should note the asymmetry of the PhC structure about the horizontal plane penetrating the center of the top Si layer in Fig. 1(d); that is, the upper surface is connected with air and the lower surface is connected with SiO_2. We therefore refer to the PhC slabs described in this section as asymmetric topological PhCs.[31)]

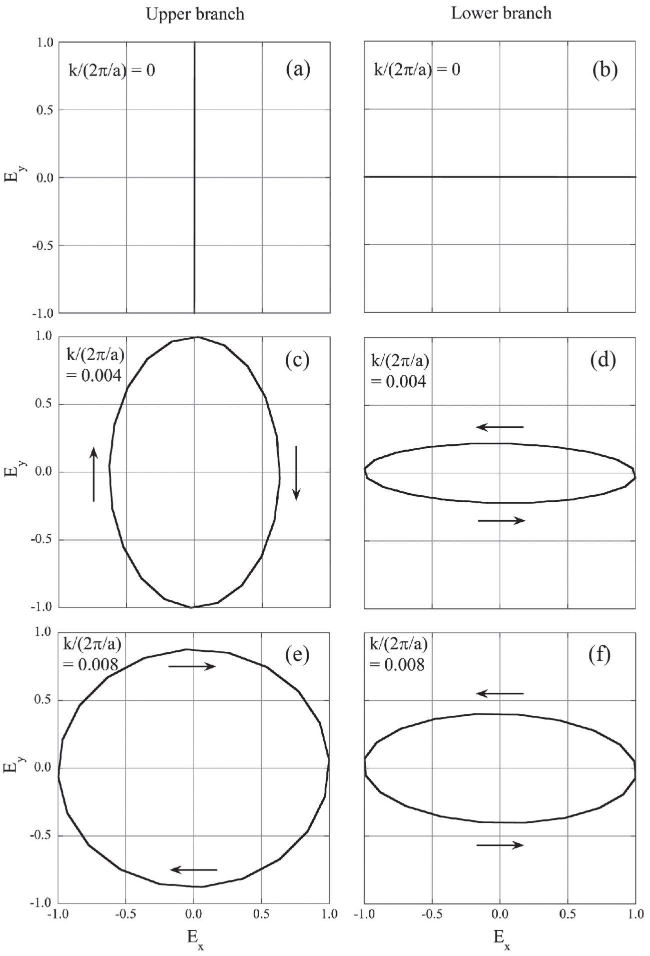

Fig. 5. Far-field polarization of the edge modes of the lower (right column) and upper (left column) branches for asymmetric topological PhCs. The far field was evaluated at $z = 16.4\,\mu\mathrm{m}$ on the border between the two PhCs. The figures show the endpoint of the electric field in the xy plane, which is normalized by its maximum value, during one period of the electromagnetic-field oscillation. Arrows show the direction of the polarization rotation. This figure is taken from Ref. 31. ©2023 The Author(s).

The Si substrate does not greatly affect the electromagnetic eigenmodes confined within the PhC provided that the thickness of the SiO_2 layers is sufficiently large. For the present case, 2-μm-thick SiO_2 is sufficient to eliminate the influence of the Si substrate on the dispersion relation of the confined modes (see Appendix of Ref. 30).

On the other hand, PhC membranes have a structural mirror symmetry about the horizontal middle plane, because both the upper and the lower surfaces are connected with air regions. As a consequence, all modes confined in the PhC have parity for this mirror plane. In fact, the TM- and TE-like modes are symmetric and anti-symmetric, respectively, in the frequency range of our interest. Then, even when topologically trivial and non-trivial PhCs with different R are located close to each other and their boundary is introduced, the whole structure is still symmetric about the horizontal middle plane. So, the parity of the eigenmodes is maintained, which means that TM-like modes and TE-like modes do not mix with each other even though the boundary destroys the structural periodicity. Therefore, the TE-like edge modes are not affected by the presence of the TM-like bulk modes in the same frequency region.

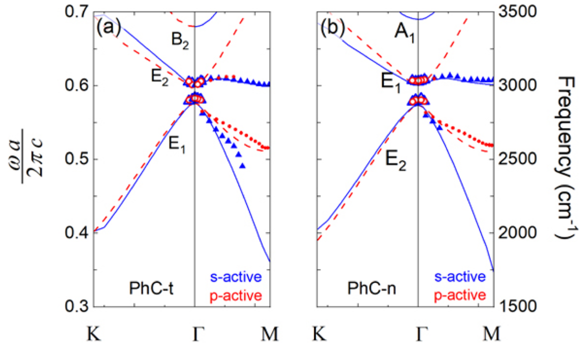

Fig. 6. (Color online) Dispersion relation of (a) symmetric PhC-t and (b) symmetric PhC-n. Broken and solid lines denote p- and s-active modes, respectively. Open circles and triangles denote eigen frequencies acquired by our home-made high-resolution setup, whereas solid circles and triangles show those measured by Seagull. Structural parameters were the same as for asymmetric topological PhCs: $a = 2.0\,\mu\text{m}$, $s = 800\,\text{nm}$, $R = 620\,\text{nm}$ for PhC-t and $R = 700\,\text{nm}$ for PhC-n. We assumed that the air cylinders were filled with SiO$_2$ and the thickness of the two SiO$_2$ layers was infinite. The latter condition was assured by introducing a PML absorbing boundary in the SiO$_2$ capping layer and 6 μm above the middle plane of the top silicon layer. On the other hand, we assumed an anti-symmetric boundary condition for the magnetic field (perfect magnetic conductor condition) on the middle plane. This condition ensured that the calculated eigenmodes were anti-symmetric TE-like modes. This figure is taken from Ref. 30. ©2023 American Physical Society.

This situation can be materialized by the symmetric PhC structure shown in Fig. 1(e), in which the upper surface of the PhC is covered with an SiO$_2$ capping layer.[30] So, we refer to PhCs of this type as symmetric topological PhCs. In the next section, we examine their sample design.

2.3 Symmetric topological PhCs

As we will describe in Sect. 3, we fabricated symmetric topological PhC specimens by EB lithography followed by plasma-enhanced chemical vapor deposition (PECVD) of the SiO$_2$ capping layer. During the latter process, the triangular air cylinders in the top Si layer were naturally filled with SiO$_2$. So, we examined this sample structure by FEM calculations. We found that a common band gap could be materialized for symmetric topological PhCs with the same structural parameters as asymmetric topological PhCs, although the width of the common band gap was smaller due to the smaller contrast of the refractive index between Si and SiO$_2$. Figure 6 shows the dispersion relation of the bulk modes of symmetric PhC-t and PhC-n. The common band gap was 4.1% wide relative to the mid-gap frequency.

The edge-mode dispersion was also obtained by numerical calculations (Fig. 7). In this figure, data points obtained by reflection measurements are also shown, which will be described in Sect. 5. As in the case of the asymmetric topological PhCs, the two edge-mode dispersion curves anti-cross each other at $k_x = 0$.

3. Sample Fabrication

We fabricated specimens by standard EB lithography and PECVD. We used Elionix ELS-125 for EB drawing, with Allresist AR-P6200 for high-contrast EB resist. The EB exposure parameters were accelerating voltage 125 kV, current 1 nA, field size 250 μm, 50,000 dots and a shot time of 0.06 μs/dot of a 240 $\mu\text{C/cm}^2$ dose. The resist pattern was developed at room temperature in xylene for 90 s, followed by an isopropyl alcohol (IPA) wash for 30 s with slow puddling. We then performed through-etching at 400 nm depth by using deep reactive ion etching (DRIE) Bosch process with 27 cycles and an etch rate of 15.14 nm/cycle. The resist residue was removed by a 20-min dip in 80 °C N-methyl-2-pyrrolidone (NMP) organic solvent, followed by an acetone wash, IPA wash, and plasma ashing.

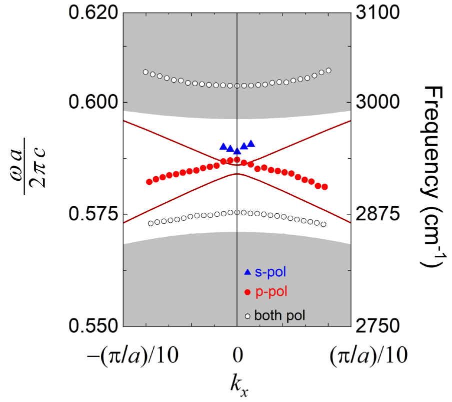

Fig. 7. (Color online) The edge-mode dispersion relation (solid lines) and the frequency range of the bulk modes (gray shading) for symmetric topological PhCs calculated by FEM, together with the mid-gap mode frequencies (closed red circles for p-active modes and closed blue triangles for s-active modes) and gap-edge mode frequencies (open circles) measured by reflection spectroscopy. This figure is taken from Ref. 30. ©2023 American Physical Society.

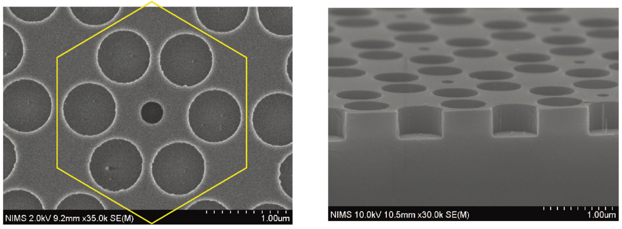

(a) (b)

Fig. 8. (Color online) SEM images of (a) top view and (b) cross-sectional view of the seven-hole PhC slab fabricated in the top silicon layer of an SOI wafer. The yellow hexagon denotes the unit cell. This figure is taken from Ref. 26. ©2022 The Author(s).

Figure 8 shows SEM images of the seven-hole PhC slab for the observation of double Dirac cones. The walls were vertically etched and the etched surface was sufficiently smooth and regular. The sample size was 3 mm × 3 mm.

Asymmetric topological PhC specimens were fabricated similarly. Their SEM images are presented in Figs. 9(a) to 9(c). Sharp vertices of the triangular holes and a consistent side length s were achieved. These sharp vertices are necessary to prevent the band gap from closing.[16,17,23] To observe the edge modes, we also fabricated a combination specimen of a 4 mm × 4 mm size composed of alternating PhC-t and PhC-n with 25 unit cells in the y direction. Figure 9(d) is an SEM image of the zigzag boundary of the combination specimen.

For symmetric topological PhCs, the samples were capped with a 2.45-μm-thick SiO$_2$ by PECVD.[30] We used tetraethyl orthosilicate (TEOS) at a flow rate of 5 sccm under 195 sccm

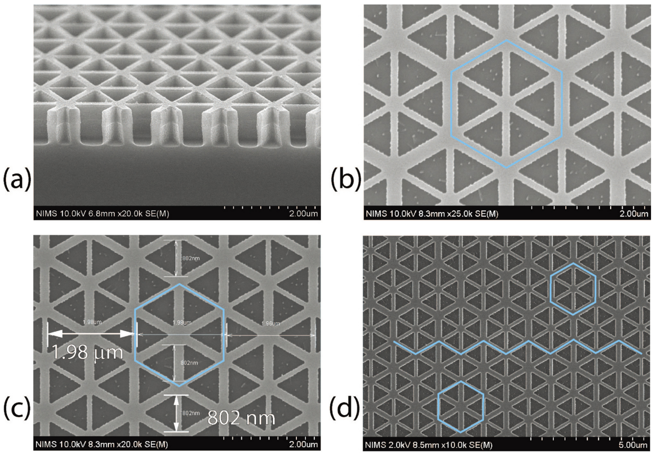

Fig. 9. (Color online) SEM images of fabricated asymmetric topological PhC specimens. (a) Cross-sectional view after etching. Top view of (b) PhC-t and (c) PhC-n. (d) Top view of the combination specimen. The zigzag boundary between PhC-t and PhC-n, as well as their unit cells, is highlighted by blue lines. This figure is taken from Ref. 31. ©2023 The Author(s).

of O_2, and we applied 50 W of RF (radio frequency) power. The substrate holder was maintained at a temperature of 350 °C throughout the deposition. During the PECVD process, the air cylinders in the top Si layer were filled with SiO_2. The air-void volume in the SiO_2 layer after the PECVD process was negligible; this was confirmed by cross-sectional SEM images and by the agreement between the designed E_1 mode frequency and its observed value.

4. Reflection Measurements

To measure the dispersion relation of the PhC specimens, we observed angle-resolved reflection spectra with an FT-IR spectrometer (JASCO FT/IR-6800). The spectral resolution was 2.0 cm^{-1}. For incident angles from 5 to 70°, we used a commercial reflection attachment, Seagull (Harrick Scientific), which was set in the sample chamber of the FT-IR. For precise measurement with smaller incident angles, the angle resolution of Seagull was not sufficient for our purpose, because Seagull used a concave mirror to focus the incident light beam on the specimen, so there was a considerable angle distribution.

We then developed our own angle-resolved reflection apparatus with a 0.3° angle resolution (Fig. 10).[34–36] All optical components were arranged on a 150 mm × 250 mm breadboard, and the breadboard was set in the FT-IR sample chamber. To compensate for the weakly focused incident beam sent from the light source of the FT-IR spectrometer, we used a pair of parabolic collimator (PM1) and parabolic condenser (PM2) to obtain a parallel beam at the sample position. Thus we achieved a 0.3° angle resolution.

Figure 11 is a photograph of our apparatus, which was set in the sample chamber of the FT-IR spectrometer. The infrared beam path is depicted by a red arrow. We also used an IR microscope (JASCO IRT-5200) to measure the normal-incidence reflection. Its angle resolution was not as high as that of our home-made apparatus due to the focusing of the incident light by the objective lens; it was estimated at 5°. For polarization-dependent reflection measurements, we used a nanoparticle-film polarizer.

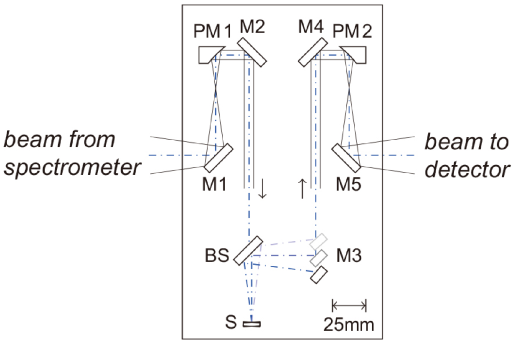

Fig. 10. (Color online) Illustration of the angle-resolved reflection apparatus. M1, M2, M4, and M5: plane mirrors; PM1: parabolic collimator; BS: beam splitter; S: rotatable sample holder; M3: movable plane mirror; and PM2: parabolic condenser (identical to PM1). The blue dash-dotted line shows the optical axis. All optical components were arranged on a 150 mm × 250 mm breadboard, depicted by the rectangular frame. This figure is taken from Ref. 34. ©2020 The Author(s).

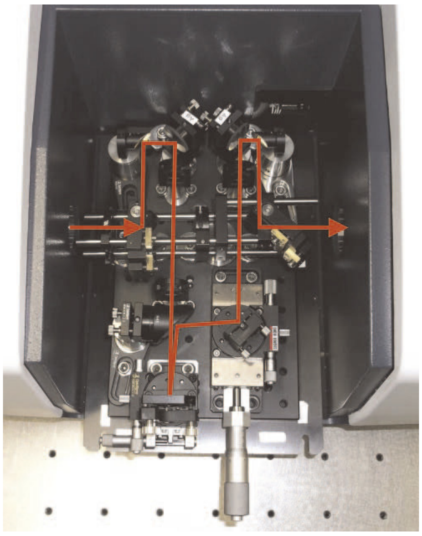

Fig. 11. (Color online) Photograph of our home-made angle-resolved reflection apparatus, which was installed in the sample chamber of the FT-IR spectrometer. The red line highlights the infrared beam path. This figure is taken from Ref. 34. ©2020 The Author(s).

5. Results and Discussions

5.1 Double Dirac cone

Figure 12 shows the angle-resolved reflection spectra of the seven-hole PhC for incident angles θ from −3.5 to 3.5° measured by our home-made apparatus. The incident light was tilted to the Γ-to-K [Figs. 12(a) and 12(b)] and Γ-to-M [Figs. 12(c) and 12(d)] directions. 25 spectra were measured for different incident angles in 0.292° steps for both the s and p polarizations. In each panel, the upper and lower limits of the lowest reflection spectrum are 1 and 0, respectively. Other spectra are drawn at the same scale and shifted by 0.1 in the vertical direction.

Each spectrum consists of two small dips overlapping a wide background peak. The former is attributed to the double Dirac cone, whereas the latter is part of broad undulations caused by multiple interference resulting from the presence of the top Si layer (400 nm thick) and the SiO_2 layer (3 μm thick). The superposition of wide and sharp resonance peaks

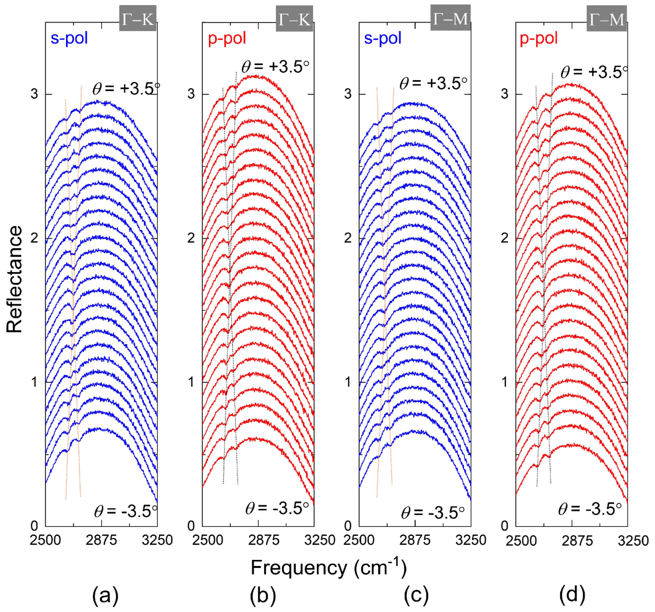

Fig. 12. (Color online) Angle-resolved reflection spectra for the seven-hole PhC. The incident beam was tilted to (a, b) the Γ-to-K direction and (c, d) the Γ-to-M direction. Two panels, for the s and p polarizations, are presented in each case. The black and orange dotted lines are drawn behind spectra to guide the eye. This figure is taken from Ref. 26. ©2022 The Author(s).

often results in a Fano-type line shape. However, this feature is not clear in Fig. 12 because the dips were too shallow and the spectral resolution of the FT-IR was not sufficient.

The shallow dips change their position linearly with θ and merge into a single dip for small incident angles ($\theta \approx 0$). All these features agree with the prediction shown in Fig. 2 and Table I. The Dirac point frequency where the two dips overlap was 2679 cm^{-1}, which is close to the designed value of 2693 cm^{-1}. Their discrepancy is only 0.56%, which proves the accuracy of our sample fabrication. The reason for the discrepancy is both the inaccuracy in the sample fabrication and the numerical calculation, the latter of which includes the ambiguity in the refractive indices assumed in the numerical calculation. Because the eigen frequency is inversely proportional to the refractive index, 1% discrepancy may occur, for example, as a result of the 1% error in the refractive index and/or in the volume percentage of the air region of the fabricated specimen. Generally speaking, we have to accept a few % discrepancy between the designed and observed eigen frequencies for specimens in the optical frequency range.

To further check the characteristics of the double Dirac cone, which was expected to be isotropic in two-dimensional **k** space, we estimated the slope (= group velocity, v_g) of the observed dispersion curves by using the dip frequencies at $\theta = \pm 2.33°$. For the four cases shown in Fig. 12, the group velocity ranged from $v_g/c = 0.254$ to 0.262, whereas the isotropic v_g/c derived from the calculated dispersion relation was 0.2555 ± 0.0032, which was obtained by averaging the slope of the dispersion curves at the Γ point in Fig. 2. These values are very close to each other and show the expected isotropy.

5.2 *Bulk modes of topological PhCs*

For topological PhCs, we first examine the dispersion relation of bulk specimens. We start with asymmetric PhCs. Figures 13(a) and 13(b) show the reflection spectra of asymmetric PhC-t and PhC-n measured by our home-made high-angle resolution apparatus for incident angles from $\theta = -3.79$ to $+4.08°$. Here we show spectra for the Γ-to-K direction. Similar spectra were observed for the Γ-to-M direction.[31)]

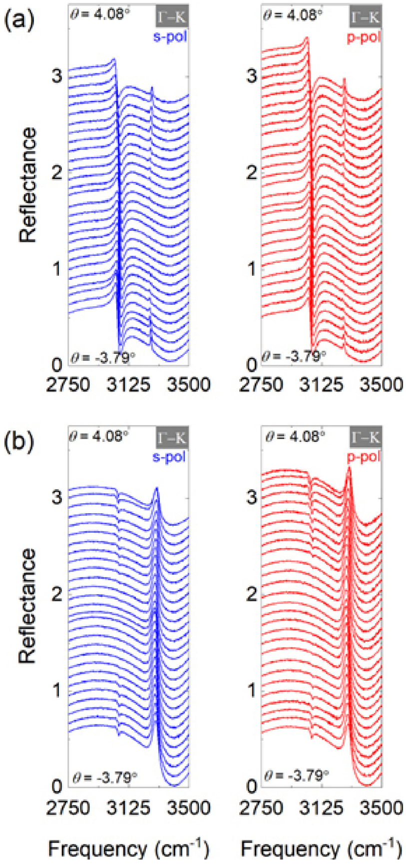

Fig. 13. (Color online) Angle-resolved reflection spectra of asymmetric (a) PhC-t and (b) PhC-n measured in the Γ-to-K direction for both the s and p polarizations by using our home-made high-resolution setup. Each panel consists of 28 spectra measured for different incident angles (θ) in 0.292° steps. The upper and lower limits of the lowest reflection spectrum in each panel are 1 and 0, respectively. Other spectra are drawn at the same scale and shifted by 0.1 in the vertical direction. This figure is taken from Ref. 31. ©2023 The Author(s).

One or two sharp peaks are superimposed on broad background undulations in each spectrum. Their line shapes are rather of the Fano type originating from the resonant reflection by the PhC eigenmodes. As we can see in the two panels of Fig. 13(a), the reflection spectra for the s and p polarizations are similar to each other, which implies that they originate from doubly degenerate eigenmodes on the Γ point, that is, the E_1 or E_2 mode. Because the higher frequency peak disappears at $\theta = 0$ and the lower frequency peak does not, we can conclude that the former is the E_2 mode and the latter is the E_1 mode for the asymmetric PhC-t by consulting Table I. Therefore, the band gap is topologically trivial. On the other hand, this feature is reversed in Fig. 13(b), so we can conclude that the band gap is topologically non-trivial for the asymmetric PhC-n, as the numerical calculations showed.

We obtained the resonance frequency by curve fitting to the observed spectrum with a combination of an asymmetric

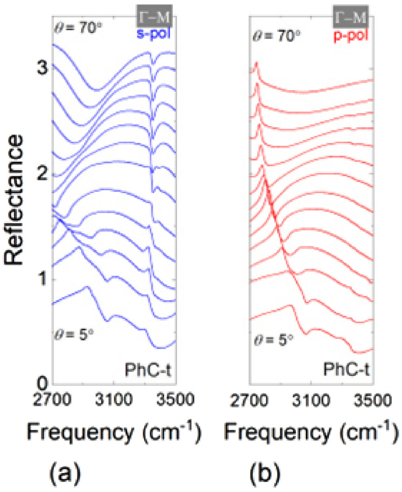

Fig. 14. (Color online) Angle-resolved reflection spectra of asymmetric PhC-t measured in the Γ-to-M direction for (a) s and (b) p polarizations by using the commercial variable-angle reflection accessory, Seagull. Each panel consists of 14 spectra measured for different incident angles (θ) in 5° steps. The upper and lower limits of the lowest reflection spectrum in each panel are 1 and 0, respectively. Other spectra are drawn at the same scale and shifted by 0.15 in the vertical direction. This figure is taken from Ref. 31. ©2023 The Author(s).

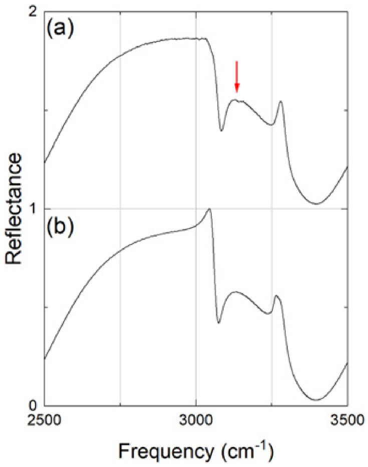

Fig. 15. (Color online) (a) Normal-incidence reflection spectrum of the combination specimen of asymmetric PhCs measured by micro FT-IR, where the red arrow points to a small dip in the common gap frequency range, which may indicate an edge mode on the Γ point. (b) Average of the normal-incidence reflection spectra of asymmetric PhC-t and PhC-n. This figure is taken from Ref. 31. ©2023 The Author(s).

Lorentzian (Fano) function for the PhC eigenmode and a polynomial function for the background undulation. We plotted the resonance frequency against the lateral components of the wave vector of the incident light to draw the dispersion curves. Thus we obtained the dispersion relation around the Γ point, as shown by the open circles and triangles in Figs. 4(a) and 4(b). The discrepancy between the calculated and observed frequencies was smaller than 0.32%, which is evidence of accurate sample fabrication.

To check that the band gap was open over the entire Brillouin zone, we measured the reflection spectra for larger incidence angles ($\theta = 5$ to 70°) with Seagull, as shown in Fig. 14 for asymmetric PhC-t in the Γ-to-M direction. By tracing the variation of peak positions with increasing θ, we can obtain the dispersion relation in this angle range. The results are plotted by the solid circles and triangles in Fig. 4(a), which shows that the frequency of the A_1 mode on the M point is higher than the E_1 and E_2 mode frequencies. Thus we confirmed that the band gap was open over the entire Brillouin zone. Similar results were obtained for the asymmetric PhC-n, as plotted in Fig. 4(b).

From Figs. 4(a) and 4(b), the trivial (PhC-t) and non-trivial (PhC-n) specimens share a common band gap from 3068 to 3257 cm^{-1}. The width of the band gap is 6.0% relative to the mid-gap frequency; this is close to the theoretical value, 5.7%, obtained in Sect. 2.

For symmetric PhC-t and PhC-n, we measured their angle-resolved reflection spectra similarly and determined their dispersion relation as shown in Fig. 6.[30] Although both the common band gap on the Γ point and the eigen frequency of the A_1 mode on the M point are smaller than the asymmetric topological PhCs due to the smaller contrast of the refractive index, the symmetric PhC-t and PhC-n share a common band gap over the entire Brillouin zone from 2917.0 to 3009.6 cm^{-1}. These values are very close to the numerical results, that is, 2882.4 to 3002.5 cm^{-1}. Their discrepancy is 1.2% at most, which is again evidence for our accurate sample fabrication.

5.3 *Edge modes*

Because the volume of the boundary between the PhC-t and PhC-n is much smaller than the bulk PhC regions, the reflection peak intensity of the edge modes is expected to be much smaller than the bulk-mode peaks. For example, Fig. 15(a) is a normal-incidence reflection spectrum of a combination specimen of asymmetric PhCs measured with the IR microscope; a small dip depicted by a red arrow is visible in the common band gap.[31] This small dip originates from the edge mode, as will be discussed below. Figure 15(b) is the average of the reflection spectra of bulk PhC-t and PhC-n as a reference. The two peaks around 3050 and 3300 cm^{-1} are the lower and upper edges of the common gap, that is, the eigen frequencies of the E_1 modes. It is apparent that the edge-mode reflection dip is much smaller than the E_1 mode peaks.

To prove that the small reflection dip originates from the edge mode, we measured its dispersion and polarization dependence with our home-made angle-resolved reflection apparatus. The measured spectra are shown in Fig. 16, where we can see spectral changes in the band-gap frequency range with varying incidence angle θ. Because the edge-mode reflection dip was small, we needed a curve-fitting procedure to obtain its accurate resonance frequency. We used three functions for the curve fitting, namely, two Fano functions for the edge mode and an E_1 mode resonance peak and a third-order polynomial for the background undulation.[31]

Figure 17 shows the measured dispersion relation of the edge modes. The solid blue triangles and red circles denote the resonance frequencies of the mid-gap modes that were detected by the s- and p-polarized incident waves, respectively, whereas the two solid green lines denote the calculated dispersion curves. Their discrepancy was as small as 1.5%. In addition, the upper and lower branches were active to the s and p polarizations at around $k_x = 0$, respectively, which agreed with the predictions shown in Figs. 5(a) and 5(b).

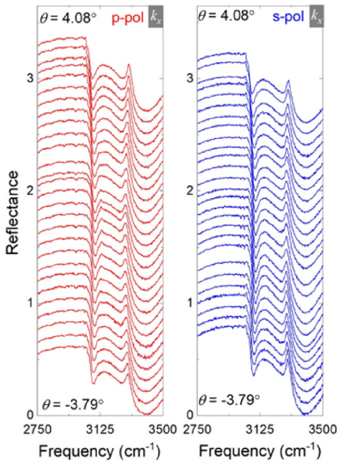

Fig. 16. (Color online) Angle-resolved reflection spectra for the combination specimen of asymmetric PhCs. Incident angles were varied from $\theta = -3.79$ to 4.08° for both the p (left panel, red) and the s (right panel, blue) polarizations. The incident beam was tilted in the x direction along the boundary between PhC-t and PhC-n. Twenty-eight spectra were measured for each polarization in 0.292° steps. The upper and lower limits of the lowest reflection spectrum are 1 and 0, respectively. Other spectra are drawn at the same scale and shifted by 0.1 in the vertical direction. This figure is taken from Ref. 31. ©2023 The Author(s).

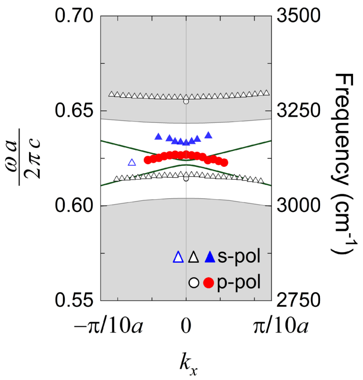

Fig. 17. (Color online) Dispersion relation of the edge modes for the asymmetric PhCs. The green lines are the calculated dispersion curves, whereas the red closed circles and blue closed triangles denote the resonance frequencies of the p- and s-active mid-gap modes, respectively. The open blue triangle denotes the lower-branch frequency detected by an s-polarized incident beam. The open black triangles and circles denote the resonance frequencies of the s- and p-active gap-edge modes, respectively, whereas the gray regions denote the calculated frequency ranges of the bulk modes. This figure is taken from Ref. 31. ©2023 The Author(s).

When $|k_x|$ becomes large, the edge-mode polarization returns to the original circular polarization. So, the edge mode becomes active to both s and p polarizations. As an example, the lower branch can also be detected by an s-polarized incident light, as evidenced by the open blue triangle at $k_x \approx -0.6 \times (\pi/10a)$.

In Fig. 17, the resonance frequencies of gap-edge modes are also plotted by open black triangles and circles. They correspond to the E_1 mode of the bulk specimens, and they correlate well with the boundaries of the bulk-mode frequencies denoted by the gray shading. However, we should note that the frequencies of the E_1 mode of the bulk specimen and the gap-edge mode of the combination specimen are generally different because the number of unit cells in the y direction is much smaller for the latter, so the eigen frequencies are shifted compared with the bulk specimen.

The edge-mode dispersion was determined similarly for the symmetric topological PhCs, which are plotted with closed blue triangles and closed red circles for the s- and p-active modes, respectively in Fig. 7.[30] They also agreed well with the calculated dispersion curves denoted by red lines. Their discrepancy was as small as 0.9%. In addition, the gap-edge modes, which are denoted by open circles, were well correlated with the boundaries of the frequency regions of the bulk modes, which are denoted by the gray shading.

6. Conclusion

In this review, we have reported the sample design, fabrication, and verification of SOI PhC slabs to materialize an electromagnetic double Dirac cone, topological PhCs, and topologically protected edge modes in the mid-IR range. We looked for these PhC slabs (non-membrane PhCs) fabricated in SOI wafers because of their ease of fabrication and their affinity for highly developed silicon photonics.

Our sample design was based on symmetry reduction from the honeycomb lattice to the C_{6v}-symmetric lattice, which resulted in relocation of the double Dirac cone onto the Brillouin zone center and the creation of topologically non-trivial band gaps. The former enabled us to observe the double Dirac cone by angle-resolved reflection spectroscopy, whereas the latter made it possible to materialize the edge modes on the boundary between the trivial and non-trivial PhCs.

To observe the dispersion relation of both the bulk and the edge modes, we developed an angle-resolved reflection apparatus that was integrated in the sample chamber of an FT-IR spectrometer. The weakly focused infrared beam from the light source of the FT-IR was compensated with a pair of parabolic mirrors to obtain a parallel beam at the sample position. Thus we achieved a 0.3° angle resolution. By applying this apparatus to precise measurement of the dispersion relation and mode symmetries around the Γ point, we verified the isotropy of the double Dirac cone and the creation of non-trivial band gaps. The linear polarization of the edge modes on the Γ point was also revealed experimentally for the first time.

The SOI PhC slabs were fabricated by EB lithography and PECVD according to the sample design by FEM calculations using commercial software COMSOL with the Wave Optics Module. The measured spectra agreed well with the calculations, which was evidence of accurate sample fabrication.

The common band gap of the topological PhCs (PhC-t and PhC-n) was created in the spectrum of TE-like modes. Although this common band gap was incomplete because of the presence of the TM-like modes in the gap frequency, we could observe the edge modes. This is most probably because the mixing between the TE- and TM-like modes was small, even when the structural periodicity was interrupted by the presence of the boundary between the PhCt and PhC-n. However, this issue needs further investigation, since incompleteness of the common band gap is a new feature unique to topological photonics.

In order to further investigate this problem, we designed and fabricated symmetric topological PhCs for which TE-TM mixing was forbidden by symmetry. We fabricated them by capping the PhC specimens with SiO_2 by PECVD. Although the width of the common band gap was smaller because of the smaller refractive-index contrast, we could materialize the edge modes for the symmetric topological PhCs and observe them by angle-resolved reflection spectroscopy.

Acknowledgments This work was supported by the Innovative Science and Technology Initiative for Security, Grant Number JPJ004596, ATLA, Japan.

---

*sakoda.kazuaki@nims.go.jp

1) Web [https://www.nobelprize.org/prizes/physics/2016/summary/] accessed on November 18, 2024.
2) Y. Hatsugai, Phys. Rev. B **48**, 11851 (1993).
3) Y. Hatsugai, Phys. Rev. Lett. **71**, 3697 (1993).
4) E. Yablonovitch, Phys. Rev. Lett. **58**, 2059 (1987).
5) S. John, Phys. Rev. Lett. **58**, 2486 (1987).
6) K. M. Ho, C. T. Chan, and C. M. Soukoulis, Phys. Rev. Lett. **65**, 3152 (1990).
7) J. D. Joannopoulos, R. D. Meade, and J. N. Winn, *Photonic Crystals: Molding the Flow of Light* (Princeton University Press, Princeton, NJ, 1995).
8) *Photonic Band Gap Materials*, ed. C. M. Soukoulis (Kluwer, Dordrecht, 1996).
9) K. Sakoda, *Optical Properties of Photonic Crystals* (Springer, Berlin, 2004) 2nd ed.
10) C. L. Kane and E. J. Mele, Phys. Rev. Lett. **95**, 226801 (2005).
11) B. A. Bernevig, T. L. Hughes, and S.-C. Zhang, Science **314**, 1757 (2006).
12) D. Hsieh, D. Qian, L. Wray, Y. Xia, Y. S. Hor, R. J. Cava, and M. Z. Hasan, Nature **452**, 970 (2008).
13) M. Z. Hasan and C. L. Kane, Rev. Mod. Phys. **82**, 3045 (2010).
14) X.-L. Qi and S.-C. Zhang, Rev. Mod. Phys. **83**, 1057 (2011).
15) L. H. Wu and X. Hu, Phys. Rev. Lett. **114**, 223901 (2015).
16) S. Barik, A. Karasahin, C. Flower, T. Cai, H. Miyake, W. D. Gottardi, M. Hafezi, and E. Waks, Science **359**, 666 (2018).
17) S. Barik, H. Miyake, W. DeGottardi, E. Waks, and M. Hafezi, New J. Phys. **18**, 113013 (2016).
18) P. D. Anderson and G. Subramania, Opt. Express **25**, 23293 (2017).
19) H. Kagami, T. Amemiya, S. Okada, N. Nishiyama, and X. Hu, Opt. Express **28**, 33619 (2020).
20) E. Sauer, J. P. Vasco, and S. Hughes, Phys. Rev. Res. **2**, 043109 (2020).
21) M. A. Gorlach, X. Ni, D. A. Smirnova, D. Korobkin, D. Zhirihin, A. P. Slobozhanyuk, P. A. Belov, A. Alù, and A. B. Khanikaev, Nat. Commun. **9**, 909 (2018).
22) N. Parappurath, F. Alpeggianil, K. Kuipers, and E. Verhagen, Sci. Adv. **6**, eaaw4137 (2020).
23) S. Okada, T. Amemiya, H. Kagami, Y. Wang, N. Nishiyama, and X. Hu, J. Opt. Soc. Am. B **39**, 2464 (2022).
24) K. Sakoda, Opt. Express **20**, 25181 (2012).
25) Y. Yao, T. Kuroda, N. Ikeda, T. Mano, H. Koyama, Y. Sugimoto, and K. Sakoda, Opt. Express **28**, 21601 (2020).
26) A. Begum, Y. Yao, T. Kuroda, E. Watanabe, N. Ikeda, Y. Sugimoto, Y. Takeda, and K. Sakoda, J. Phys. Soc. Jpn. **91**, 084401 (2022).
27) P. L. Gourley, J. R. Wendt, G. A. Vawter, T. M. Brennan, and B. E. Hammons, Appl. Phys. Lett. **64**, 687 (1994).
28) O. Painter, R. K. Lee, A. Scherer, A. Yariv, J. D. O'Brien, P. D. Dapkus, and I. Kim, Science **284**, 1819 (1999).
29) T. Kuroda, N. Ikeda, T. Mano, Y. Sugimoto, T. Ochiai, K. Kuroda, S. Ohkouchi, N. Koguchi, K. Sakoda, and K. Asakawa, Appl. Phys. Lett. **93**, 111103 (2008).
30) A. Begum, Y. Yao, T. Kuroda, Y. Takeda, N. Ikeda, Y. Sugimoto, T. Mano, and K. Sakoda, Phys. Rev. A **107**, 043507 (2023).
31) A. Begum, Y. Yao, T. Kuroda, Y. Takeda, N. Ikeda, Y. Sugimoto, T. Mano, and K. Sakoda, J. Phys. Soc. Jpn. **92**, 114402 (2023).
32) D. Chandler-Horowitz and P. M. Amirtharaj, J. Appl. Phys. **97**, 123526 (2005).
33) I. H. Malitson, J. Opt. Soc. Am. **55**, 1205 (1965).
34) T. Kuroda, S. Chalimah, Y. Yao, N. Ikeda, Y. Sugimoto, and K. Sakoda, Appl. Spectrosc. **75**, 259 (2021).
35) Y. Yao, N. Ikeda, T. Kuroda, T. Mano, H. Koyama, Y. Sugimoto, and K. Sakoda, Opt. Express **28**, 4194 (2020).
36) S. Chalimah, Y. Yao, N. Ikeda, K. Kaneko, R. Hashimoto, T. Kakuno, S. Saito, T. Kuroda, Y. Sugimoto, and K. Sakoda, Phys. Rev. Appl. **15**, 064076 (2021).

Yuanzhao Yao was born in 1982 in Tianjin, China. He received his Ph.D. in 2018 from the University of Tsukuba, Japan. After completing a four-year postdoctoral research position at the National Institute for Materials Science (2018–2022), he joined the Department of Applied Physics at the University of Tsukuba in 2022. Since 2024, he has been an assistant professor at the University of Tsukuba. His research focuses on the electromagnetic field analysis of photonic crystals and the analysis of image formation processes in scanning electron microscopy (SEM) using simulation techniques.

Afshan Begum was born in Bangalore (India), received her Ph.D. from the University of Tsukuba (Japan) in materials science and engineering, for the study on electromagnetic double Dirac cones and topological edge modes in photonic crystal slabs in 2023. She contributed to the first observation of photonic double Dirac cones by high-precision nanofabrication of photonic crystal arrays. She is a postdoctoral researcher in the Quantum Photonics Group at National Institute for Materials Science, Japan, contributing to the development of photonic crystals for semiconductor lasers. Her research interests are to efficiently and precisely control light by improving semiconductor nanofabrication for photonics and optical waveguides to advance optical telecommunication devices.

Naoki Ikeda received his B.S. (1998) degree from Tokyo University of Science. After working on research into semiconductor nano-fabrication technology and photonic crystal optical devices at Femtosecond Technology (1998–2004) and National Institute of Advanced Industrial Science and Technology (2004–2007), he obtained his D.Eng. (2007) degrees from the University of Tsukuba. He joined the National Institute for Materials Science in 2007 and currently supports research in a variety of fields using semiconductor microfabrication technology.

Yoshihiko Takeda was born in Nagano Prefecture, Japan, in 1963. He obtained his B.S. (1986), M.S. (1988), and Ph.D. (1995) degrees from Tohoku University. He worked at the Thin Film Laboratory and the Recording Media Laboratory of Teijin Limited (1988–1996). He was a researcher (1996–1999), a senior researcher (1999–2003), a principal researcher (2003–2007), a chief researcher (2007–2011), and a group leader (2011–2025) at NRIM/NIMS. He was concurrently an associate professor (2004–2011) and a professor (2011–2025) at NIMS's collaborative graduate program in the University of Tsukuba. Since 2025, he has been a NIMS special researcher at NIMS. His research primally focuses on fabrication of nanostructures and surface modification by high-current heavy-ion irradiation techniques, and applications to nanooptics.

Takashi Kuroda was born in Hokkaido in 1967. He obtained his B.S. (1990), M.S. (1992), and Ph.D. (1994) degrees from Hokkaido University. He was a research associate at Tokyo Institute of Technology (1995–2003) and a senior/principal/chief researcher at NIMS (2003–). Currently, he is a group leader of Quantum Photonics Group at NIMS and an adjunct professor at Kyushu University. His research focuses the development of high-precision laser spectroscopy techniques and their application to the study of quantum materials.

Kazuaki Sakoda was born in Kyoto in 1957. He received his B.E. (1980), M.E. (1982), and Ph.D. (1992) degrees from Tokyo University. He worked for Toray Industries as a senior researcher (1982–1992). He was an associate professor at Research Institute for Electronic Science, Hokkaido University (1993–2002). He moved to National Institute for Materials Science, Tsukuba in 2002. He was the director of Quantum Dot Research Center (2007–2011) and Photonic Materials Unit (2011–2016) there. He was concurrently a professor at NIMS's collaborative graduate program in the University of Tsukuba (2004–2018). He has mainly been engaged in the study of nanophotonics in general and the theoretical study of photonic crystals in particular.